

Airborne Measurements of Surface Wind and Slope Statistics over the Ocean

LUC LENAIN, NICHOLAS M. STATOM, AND W. KENDALL MELVILLE

Scripps Institution of Oceanography, University of California, San Diego, La Jolla, California

(Manuscript received 22 April 2019, in final form 19 July 2019)

ABSTRACT

As reported in 1954, more than a half century ago, C. Cox and W. Munk developed an empirical model of the slope distribution of ocean surface waves that has been widely used ever since to model the optical properties of the sea surface and is of particular importance to the satellite remote sensing community. In that work, the reflectance of sunlight was photographed from a Boeing B-17G bomber and was then analyzed. In this paper, surface slope statistics are investigated from airborne scanning topographic lidar data collected during a series of field experiments off the coast of California and in the Gulf of Mexico, over a broad range of environmental conditions, with wind speeds ranging from approximately 2 to 13 m s⁻¹. Unlike the reflectance-based approach of Cox and Munk, the slope distribution is computed by counting laser glints produced by specular reflections as the lidar is scanned over the surface of the ocean. We find good agreement with their measurements for the mean-square slope and with more recent (2006) results from Bréon and Henriot that were based on satellite remote sensing. Significant discrepancies for the higher-order statistics are found and discussed. We also demonstrate here that airborne scanning lidar technology offers a viable means of remotely estimating surface wind speed and momentum flux.

1. Introduction¹

Better understanding and modeling of the sea surface roughness are of critical importance for remote sensing studies and measurements of air–sea fluxes. Wind roughens the ocean surface, producing short gravity–capillary waves, breaking waves, and foam. When combined with accurate surface slope models, the scattering of microwave radar signals over these complex surfaces provides a way to estimate surface wind speed remotely and globally (e.g., [Fung et al. 2010](#)). Sun glints, caused by the specular reflections of direct solar radiance from the sea surface, have a significant impact on remotely sensed ocean color, reflectance, and surface temperature observations and need to be correctly accounted for (e.g., [Gordon and Wang 1992, 1994](#)).

The seminal work of [Cox and Munk \(1954\)](#) was the first attempt to derive an ocean surface slope distribution model, based on a limited number of sun-glitter photographs collected from a U.S. Air Force Boeing B-17G aircraft off the coast of Maui, Hawaii, to estimate surface slope probability density functions (pdfs). Their empirical approach consisted of fitting their optical measurements of sun-glitter patterns to a Gram–Charlier series and relating their statistics to in situ measurements of wind speed collected from the 58-ft-long (1 ft = 30.5 cm) schooner *Reverie*, positioned at the experiment site. This work found renewed interest several decades later with the development of scatterometers and microwave radars that were used to estimate the surface wind speed, where the modeling of the ocean surface slope distribution is an essential component of the measurement technique.

Surprisingly, in part because of the complexity and observational challenges characterizing surface slope distributions, only a few studies attempted to revisit these results since then. Several authors ([Hughes et al. 1977](#); [Haimbach and Wu 1985](#); [Hwang and Shemdin 1988](#); [Shaw and Churnside 1997](#)) used field observations from a refractive laser slope gauge and a reflective scanning laser to compute slope statistics and found

¹ This paper is dedicated to the memory of our Scripps colleagues “Chip” Cox (1922–2015) and Walter Munk (1917–2019).

 Denotes content that is immediately available upon publication as open access.

Corresponding author: Luc Lenain, llenain@ucsd.edu

DOI: 10.1175/JPO-D-19-0098.1

© 2019 American Meteorological Society. For information regarding reuse of this content and general copyright information, consult the [AMS Copyright Policy](#) (www.ametsoc.org/PUBSReuseLicenses).

a linear relationship between the mean-square slope and wind speed, as in [Cox and Munk \(1954\)](#). [Su et al. \(2002\)](#) used a scanning spectral photometer from a coastal ocean platform and [Gatebe et al. \(2005\)](#) used the Cloud Absorption Radiometer (CAR) from a research aircraft to investigate sun glint and its relation to slope distribution. Some of these studies hinted at the role played by atmospheric stability (e.g., [Shaw and Churnside 1997](#); [Haimbach and Wu 1985](#)) in modeling surface slope distributions, based on limited datasets, which therefore restricted their range of applicability.

[Bréon and Henriot \(2006\)](#) used satellite remote sensing products from the U.S. National Aeronautics and Space Administration (NASA) Scatterometer (NSCAT) and the Polarization and Directionality of the Earth's Reflectances (POLDER) to compute slope pdfs using the same approach developed by [Cox and Munk \(1954\)](#). They found a remarkable agreement with their results, especially for the mean-square slope, as highlighted in the [Munk \(2009\)](#) review.

Recently, the development of polarimetric imaging technology ([Zappa et al. 2008, 2012](#); [Laxague et al. 2015](#); [Kiefhaber et al. 2015](#)) has provided a new method to characterize slope distributions. The measurement technique itself is particularly challenging, because the incoming light polarization has to be accurately known to obtain valid slope measurements. All of these studies show mean-square slopes of lower magnitude than the [Cox and Munk \(1954\)](#) model, explained at times by the possible presence of surfactants at the experiment site where the polarimetric measurements were collected. Surfactant layers are known to have a dramatic impact on the surface wave properties. These layers reduce surface roughness² and are therefore of importance for air–sea interaction processes, because shorter waves support most of the momentum flux between the ocean and the atmosphere.

It is remarkable that, in the latter part of their incredible scientific careers, and more than 50 years after their original study was published, both Cox and Munk had returned to the study of the slope statistics of the sea surface, also referred to as the “sun-glitter problem.” Cox’s interest was geared toward a better understanding of the underlying physics of wave–surfactant interactions. In a 2015 maritime history research note, he recounted the rescue of the crew of a sinking ship in the early 1880s (the *Grecian*) that used fish oil to suppress breaking waves during a severe storm and enabled the crew to transfer to the rescue

ship *Martha Cobb* ([Cox 2015](#)). These historical records provided the basis for a wave energy model that incorporates the reduced roughness caused by the oily surface film ([Cox et al. 2017](#)).

For the last decade Munk was revisiting the topic, leading to a review paper on sea surface slope statistics ([Munk 2009](#)), comparing the mean-square slope results of [Cox and Munk \(1954\)](#) with the satellite-derived results of [Bréon and Henriot \(2006\)](#). The lack of existing theory that would explain the linear wind dependence of the mean-square slope and its unexpectedly large crosswind component was of particular interest to him, and he proposed that such directional spreading could be produced by localized sources that could generate obliquely propagating “ship wake”-like waves. He concluded his review by recalling earlier discussions on the topic and provided some insight:

At the 1955 celebration of the 25th birthday of the Woods Hole Oceanographic Institution, I was given the opportunity to review what was then known about our subject ([Munk 1955](#)). After referring to the Cox and Munk result of a linear wind dependence of the mean-square slope and its large crosswind component, I spoke of the need for “a respectable theory” of wind drag, and, referring to a recent photograph, mentioned “how important it is to look at the raw data before deciding on pertinent statistical parameters.” How slow progress has been in the past fifty years!

But there is hope. I surmise that the key contributing wave scales range from millimeters to a meter. These are the very scales that will be the subject during the next few years of extensive sea-going experiments, which will use powerful new optical tools. If the time for review is when a subject is under active development, with new solutions being found and old solutions being demolished, not when it is to be tidied and put to rest, then this is indeed the right time for review.

To this end, no theory has been brought forward that would explain such surface slope statistics.

In the current study, we characterize and investigate the properties of ocean surface slopes measured during a series of experiments off the coast of California and the Gulf of Mexico from an airborne scanning lidar installed on a research aircraft. The experiment, instrumentation, environmental conditions, and processing techniques are presented in [section 2](#). [Section 3](#) describes the results in the context of the work of [Cox and Munk \(1954\)](#) and discusses the potential application of this technique for airborne remote sensing of surface wind speed and momentum flux. The findings are summarized in [section 4](#).

² Surface roughness is mostly produced by very short, gravity–capillary waves.

2. Experiments

Data presented here were collected during multiple experiments: the Office of Naval Research (ONR) Departmental Research Initiative (DRI) Radiance in a Dynamic Ocean 2008 (RaDyO2008) project (Dickey et al. 2012); the Gulf of Mexico 2011 (GoMEX2011; Romero et al. 2017) experiment; Southern California 2013 (SOCAL2013), one of the High Resolution (HIRES, or HiRes) ONR DRI field efforts (Lenain and Melville 2017; Grare et al. 2018); the recent Langmuir Circulation and Inner Shelf ONR DRI field efforts (LCDRI2017 and ISDRI2017, respectively); and a NASA–JPL-funded project to collect airborne lidar altimetry data under “AltiKa” (a Ka-band altimeter) satellite tracks off the coast of Monterey, California, to validate the NASA–JPL Air Surface Water and Ocean Topography (AirSWOT) instrument (April 2015).

Note that the present study is primarily based on the SOCAL2013 and LCDRI2017 projects in which phase-resolved measurements of wind and waves over a broad range of environmental conditions were collected. Both of these experiments were located between San Clemente and San Nicholas Islands (vicinity of 33°13.202'N, 118°58.767'W) where the floating ocean research platform R/P *Floating Instrument Platform (FLIP)* was moored, from 7 to 22 November 2013 and 16 March to 10 April 2017, for the SOCAL2013 and LCDRI2017 experiments, respectively. The R/P *FLIP* was instrumented with a suite of sensors described below to characterize the atmospheric, surface, and subsurface conditions at the experiment site. A combined total of 18 research flights are considered in the analysis, corresponding to 51.7 h of on-station flight in the vicinity of the in situ measurements.

a. The Modular Aerial Sensing System

Spatiotemporal measurements of the sea surface topography and surface kinematics were collected from a Partenavia P68 aircraft that was instrumented with the Modular Aerial Sensing System (MASS), an instrument package developed at Scripps Institution of Oceanography (Melville et al. 2016).

At the heart of the system, and of specific interest for this study, a Riegl Laser Measurement Systems GmbH model Q680i waveform scanning lidar is used to make spatiotemporal measurements of the sea surface. The sensor has a maximum pulse repetition rate of 400 kHz and a maximum line scan rate of 200 Hz, and it has been used at altitudes up to 1500 m with sufficient returns for surface-wave measurements. Because of a $\pm 30^\circ$ cross-heading scan-angle envelope, the theoretical swath

width over water is proportional to the altitude of the aircraft,³ with its effective width being dependent on the wind speed and sea state. More details are available in Melville et al. (2016).

The MASS is also equipped with a 14-bit, 640×512 pixel-resolution quantum well infrared photodetector (QWIP) forward-looking infrared (FLIR) FLIR Systems, Inc., model SC6000 infrared camera operating at up to a 126-Hz frame rate in the 8.0–9.2- μm spectral band range, to measure the ocean surface temperature field including modulations and gradients due to fronts, surface signatures of Langmuir circulation and wave breaking (Sutherland and Melville 2013). A hyperspectral camera [Spectral Imaging, Ltd. (SPECIM) model AISAEagle] operating in the 400–990-nm spectral band (from visible to near-IR) and a Jai, Ltd./Pulnix Sensors, Inc., model AM-800CL (3296×2472 pixel resolution) monochrome (12 bit) video camera that operates at a frame rate of up to 17 Hz are used to provide visible imagery of the kinematics of whitecaps (Melville and Matusov 2002; Kleiss and Melville 2010, 2011; Sutherland and Melville 2013).

All data collected are carefully georeferenced from the aircraft to an Earth coordinate frame using a NovAtel, Inc., model SPAN-LN200, a very accurate GPS–inertial measurement unit (IMU) system combining GPS technology with an IMU using fiber-optic gyroscopes and solid-state accelerometers to provide position and attitude data at up to 200 Hz. After differential GPS processing, using NovAtel Waypoint Inertial Explorer software, the stated accuracy for the instrument position is 0.01 m in the horizontal plane and 0.015 m in the vertical direction, with attitude accuracies of 0.005°, 0.005°, and 0.008° for roll, pitch, and heading, respectively. A calibration–validation flight over stationary targets is conducted prior to and after each campaign to minimize boresight errors that are due to the misalignment between the GPS–IMU system and the lidar (Melville et al. 2016). Once calibrated, we typically find absolute vertical errors of 2–4 cm (per lidar pulse) for the final topographic product, estimated at 2.3 and 2.1 cm in this study from the calibration flight conducted prior to and after each experiment.

Note that an earlier version of the MASS was used during the RADYO2009 experiment. The instrument package was built around a Riegl LMS Q240i airborne scanning lidar. This system uses a 905-nm class-I laser, with a beam divergence of 2.7 mrad and an 80° field of view. The laser has a pulse repetition rate of

³ The swath width is close in value to the aircraft altitude.

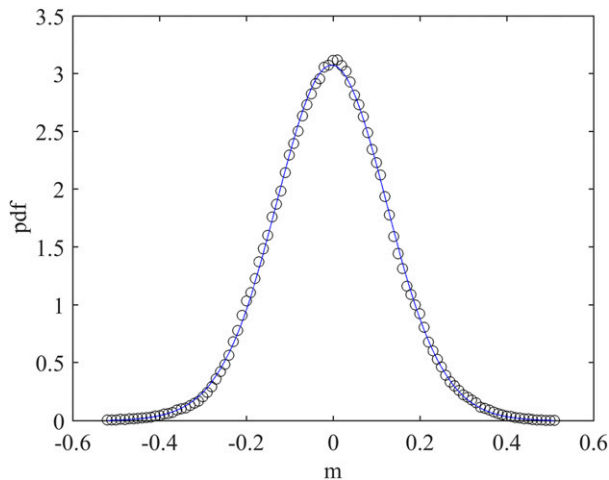


FIG. 1. Measured along-wind slope pdf (black circles); shown are data collected during the SOCAL2013 experiment and the corresponding fit (blue line) using a Gram-Charlier series.

30 kHz and a line scan rate of 30 Hz. The instrument is collocated with a Coda Octopus Products, Ltd., F180 dual-antennae GPS-IMU to provide position and attitude information. Detailed performance and specification information are presented in Reineman et al. (2009).

b. Environmental conditions

A suite of atmospheric sensors was installed on R/P *FLIP*'s port boom to characterize the marine atmospheric boundary layer variables used in the analysis. During SOCAL2013, the wind speed and direction were measured from a sonic anemometer (Gill Instruments, Ltd., model R3-50) mounted on a vertically oriented telescopic mast that was deployed from the end of the horizontally extended 20-m-long port boom of *FLIP*, at a height ranging from approximately 5 down to 2.65 m above mean sea level (MSL), and from two Campbell Scientific, Inc., model CSAT3 anemometers installed at fixed heights of 8.5 and 14.5 m MSL. The height of the anemometers above mean sea level varied during the course of the experiment depending on environmental conditions (Grare et al. 2018) but was typically in the range of 2.6–4 m MSL for the lowest sensor, the Gill R3-50. During LCDRI2017, two ultrasonic anemometers (Gill R3-50) were installed at fixed heights of 8.3 and 14 m MSL.

The friction velocity u_* in the air is given by

$$u_* = (\overline{u'w'^2} + \overline{v'w'^2})^{1/4}, \quad (1)$$

where u , v , and w represent the three components of the wind vector in the along, cross, and vertical directions, respectively, and the prime denotes that

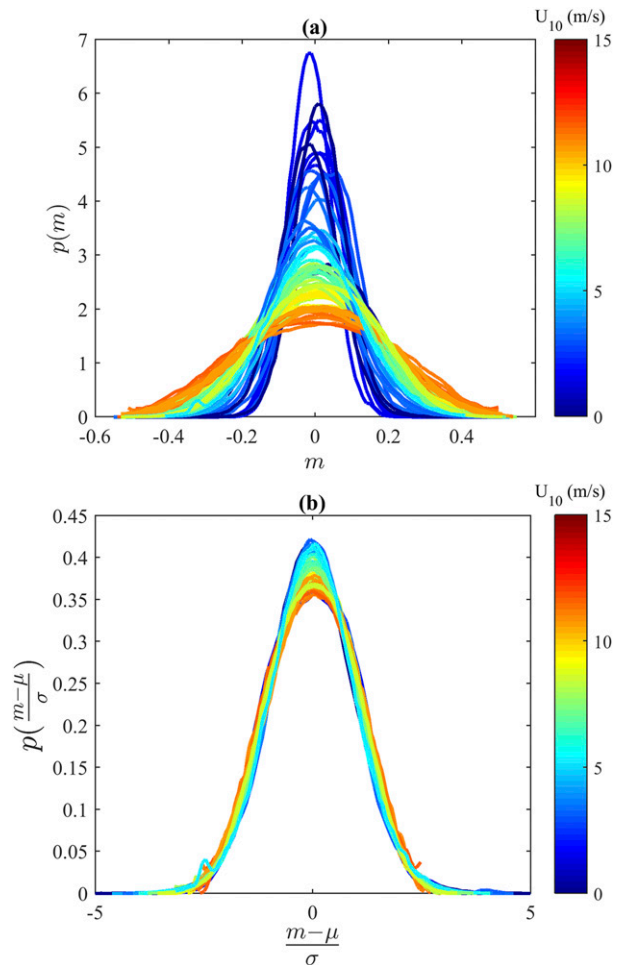


FIG. 2. (a) Lidar-measured along-wind slope color coded for in situ wind speed data U_{10} from the SOCAL2013 and LCDRI2017 experiments. (b) The same data, but scaled by the standard deviation and mean of the pdfs.

component quantities have had their mean removed. The covariances $\overline{u'w'}$ and $\overline{v'w'}$ are computed over 30-min records from the average cospectra for (u', w') and (v', w') .

The wind speed U_{10} at 10-m height above the ocean surface was interpolated between the data collected at the measurement heights closest to the ocean surface, approximately 8.5 and 14.5 m MSL, assuming a constant flux layer with a logarithmic wind profile.

c. Satellite remote sensing

In addition to the in situ atmospheric data collection from R/P *FLIP*, remotely sensed wind from two satellite altimeters are considered here. The first one, the *Satellite with Argos and AltiKa* (SARAL/AltiKa), which is a cooperative mission between the Indian Space Research Organization (ISRO) and Centre National d'Etudes

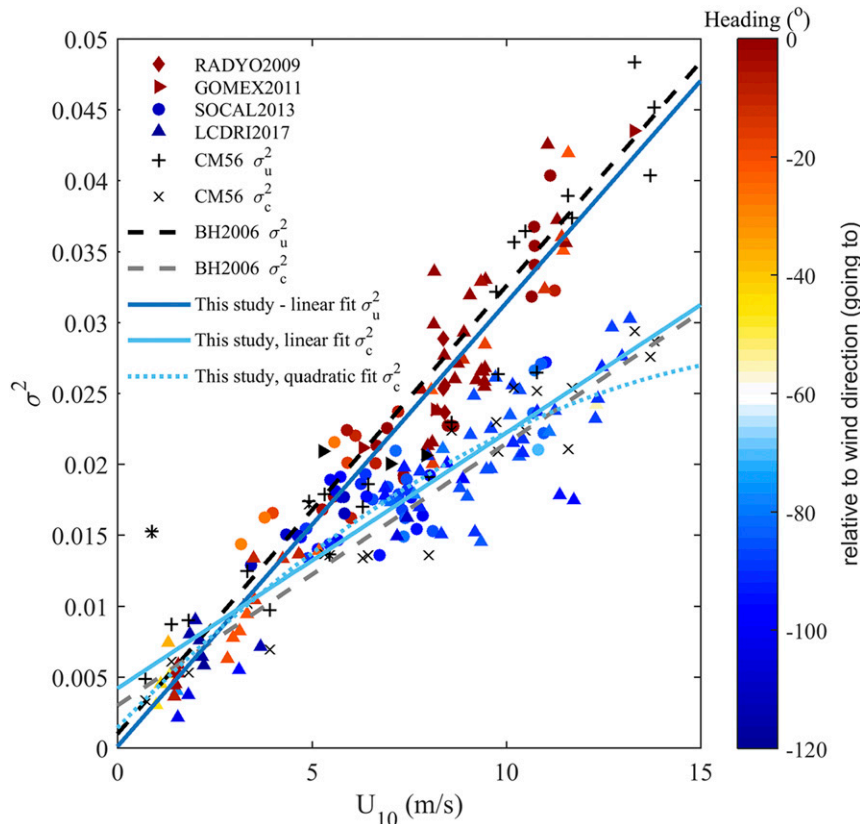


FIG. 3. Mean-square slope σ^2 computed from the airborne lidar during four distinct experiments (RADYO2009, GOMEX2011, SOCAL2013, and LCDRI2017), color coded for their heading relative to the mean wind direction, along with the data from Cox and Munk (1954, 1956) (label CM56), and Bréon and Henriot (2006) (label BH2006) as a function of wind speed U_{10} . Fits are shown with solid and dashed lines.

Spatiales (CNES), is equipped with a Ka-band radar altimeter operating at 35.75 GHz and a two-channel microwave radiometer operating at 23.8 and 37.0 GHz. The wind speed is computed from the Ka-band reflected power, or backscatter coefficient, combined with an empirical wind model (Lillibridge et al. 2014). The second satellite considered here is *Jason-1*, a joint mission between CNES and NASA. The approach is the same to derive the wind speed, although this time Ku- and C-band frequencies are used (see, e.g., Ménard et al. 2003; Abdalla 2012).

d. Using lidar to measure surface slope statistics

Shaw and Churnside (1997) first introduce the concept of using the “laser-glint-meter technique” to compute slope statistics. The basic idea is to count laser glints from specular reflections as a laser or lidar is scanned over the surface of the ocean. In the context of using an airborne lidar to measure sea surface slope statistics, the issue of interpreting the return signals from the lidar pulses arises.

Assuming for the present an idealized 1D case in which the scattering of the lidar pulse from the surface is specular, the footprint size of the emitted lidar pulse on the surface is sufficiently small, and the range of sea surface slopes is $\pm \mathcal{M}$, then the probability that the slope is in the range from $-\mathcal{M}$ to \mathcal{M} is unity. In one data record i (say for a constant wind speed) assume that n_{pi} pulses are transmitted in the angle increment $m_i \pm \Delta m/2$, resulting in n_{ri} received return signals. We define N_p and N_r as the total number of pulses transmitted and received, respectively, such that

$$N_p = \sum_{i=1}^N n_{pi} \quad \text{and} \quad (2)$$

$$N_r = \sum_{i=1}^N n_{ri}. \quad (3)$$

Here N is defined such that $N\Delta m = 2\mathcal{M}$.

The probability that the slope is in $m_i \pm \Delta m/2$ is given by

$$p(m_i)\Delta m = \frac{n_{ri}}{N_r} = \frac{n_{ri} n_{pi} N_p}{n_{pi} N_p N_r}, \quad (4)$$

where $p(m_i)$ is the discrete pdf. As required for a pdf,

$$\sum_{i=1}^N p(m_i)\Delta m = \frac{1}{N_r} \sum_{i=1}^N n_{ri} = 1, \quad (5)$$

and in the continuous limit we have

$$\int_{-\mathcal{M}}^{+\mathcal{M}} p(m) dm = 1. \quad (6)$$

The ratio n_{pi}/N_p is a tunable constant of the lidar as well as Δm , and the ratio N_p/N_r is a measurable integral parameter for each data record. Therefore, we can write Eq. (5) as

$$p(m_i)\Delta m = C(n_{ri}/n_{pi}), \quad (7)$$

where

$$C = \frac{n_{pi} N_p}{N_p N_r} \quad (8)$$

is a measurable parameter for each environmental state.

3. Results

a. Slope probability density functions

A representative example of along-wind slope pdf $p(m)$ computed from the MASS lidar data is shown in Fig. 1. The data used to estimate the pdf were collected during the SOCAL2013 experiment; 10-km-long swaths flown in a cross-wave direction are considered. An empirical altitude correction is applied to the measurements to account for changes in laser footprint and associated multipath returns that are not considered in the specular reflection assumption described above. This correction is described in the appendix.

Also shown in Fig. 1 is a fit to a Gram–Charlier series, as suggested by Cox and Munk (1954), and defined as

$$p\left(\frac{m-\mu}{\sigma}\right) = \sum_{n=0}^{N_s} \frac{c_n}{n!} H_n\left(\frac{m-\mu}{\sigma}\right) G\left(\frac{m-\mu}{\sigma}\right), \quad (9)$$

where μ and σ represent the mean and standard deviation of the measured pdf, respectively; $G()$ is a zero-mean unit-variance Gaussian distribution; $H_n()$ are the n th-order Hermite polynomials (Papoulis and Pillai 2002), and c_n are expansion coefficients obtained by fitting the measured distribution. Here the expansion series to

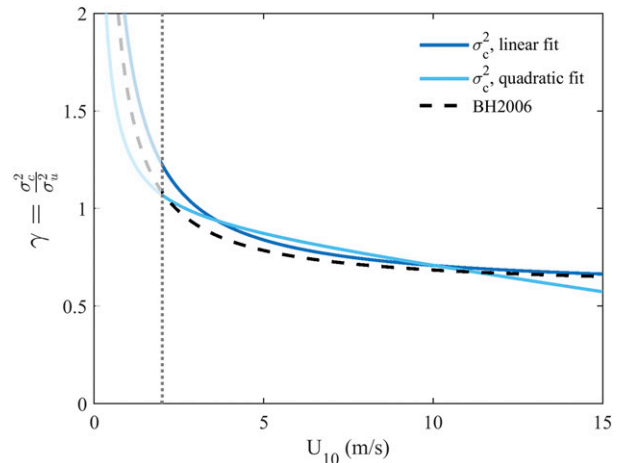


FIG. 4. The ratio of crosswind to upwind mean-square slope $\gamma = \sigma_c^2/\sigma_u^2$ as a function of U_{10} , using both linear [Eq. (13)] and quadratic fits for the crosswind direction. Note that this ratio is only valid for winds that are larger than approximately 2 m s^{-1} , represented by a vertical gray dotted line.

$N_s = 4$ was used because the higher-order terms were found to be statistically insignificant.

b. Mean-square slope

Figure 2a shows all along-wind slope pdf p collected during the SOCAL2013 and LCDRI2017 experiments, color coded for wind speed U_{10} measured from R/P FLIP. The maximum value of the pdfs, near nadir (where $m \approx 0$), is found to be inversely proportional to the value of U_{10} , and the distribution widths of the pdfs get broader for higher wind speeds. The same pdfs are presented in Fig. 2b, this time as a function of nondimensionalized slope $(m - \mu)/\sigma$. These scaled pdfs generally collapse onto a single pdf curve, with more variability closer to nadir and with a maximum magnitude that is inversely proportional to wind speed. The range of nondimensionalized slope $(m - \mu)/\sigma$ that we are able to characterize extends from -5 to 5 .

The mean-square slope σ^2 is shown in Fig. 3, plotted against wind speed U_{10} and color coded for the heading relative to the measured wind direction β . Dark-red points represent upwind components, and blue points represent crosswind ones. Also shown are the airborne measurements from Cox and Munk (1954, 1956) and parameterizations derived from satellite remote sensing products (POLDER mission; Deschamps et al. 1994) analyzed in Bréon and Henriot (2006). Here β is computed using the wind direction measured on FLIP and the mean heading of the lidar swath over the segment considered in the computation, and not the aircraft heading, since at

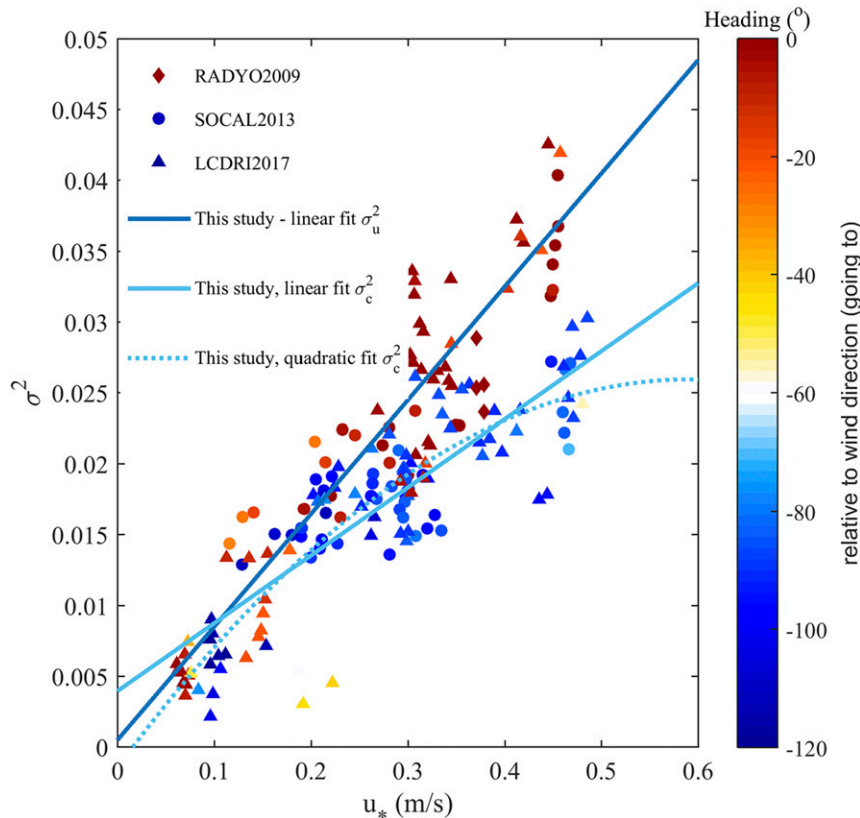


FIG. 5. Mean-square slope σ^2 computed from the airborne lidar during four distinct experiments (RADYO2009, GOMEX2011, SOCAL2013, and LCDRI2017), color coded for their heading relative to the mean wind direction, as a function of friction velocity u_* . Fits are shown with solid and dashed lines.

times—especially during crosswind flights—the aircraft experienced significant “crab” angles (difference between aircraft heading and course angles; up to 35° in this study). The upwind mean-square slope σ_u^2 is taken as all of the measurements collected within $\pm 30^\circ$ of the wind direction, and the crosswind counterparts σ_c^2 correspond to all of the measurements collected within $\pm 30^\circ$ of the crosswind direction. Linear fits are computed for both upwind and crosswind components, giving

$$\sigma_u^2 = 3.13 \times 10^{-3} U_{10} + 1.1 \times 10^{-4} \quad \text{and} \quad (10)$$

$$\sigma_c^2 = 1.8 \times 10^{-3} U_{10} + 4.2 \times 10^{-3}. \quad (11)$$

Note that for low values of U_{10} the crosswind measurements appear to converge toward zero and are therefore better represented by the following quadratic fit

$$\sigma_c^2 = -7.6 \times 10^{-5} U_{10}^2 + 2.84 \times 10^{-3} U_{10} + 1.43 \times 10^{-3}. \quad (12)$$

Overall, we find a good agreement with the estimates of Bréon and Henriot (2006) and measurements of Cox and Munk (1954) from these lidar-based estimates of mean-square slope.

The ratio $\gamma = \sigma_c^2 / \sigma_u^2$, which is a measure of the directionality of the total surface slope, is shown in Fig. 4 using both linear and quadratic fits described above. Assuming a linear fit for the crosswind component, we find, for wind speeds ranging from 2 to 13 m s^{-1} , that

$$\gamma = \frac{\sigma_c^2}{\sigma_u^2} = 0.5752 + \frac{1.32}{U_{10}} - \frac{0.0431}{U_{10}^2}. \quad (13)$$

Above $2\text{--}3 \text{ m s}^{-1}$ wind speeds, the ratio is less than 1, suggesting anisotropy in the directionality of the mean-square slope once the wind starts picking up. We find $\gamma = 0.71$ for $U_{10} = 10 \text{ m s}^{-1}$, consistent with Cox and Munk (1954) and Bréon and Henriot (2006), who found $\gamma = 0.8$ and $\gamma = 0.66$, respectively, for the same wind speed.

Figure 5 shows the mean-square slope σ^2 as a function of friction velocity u_* for three experiments in which

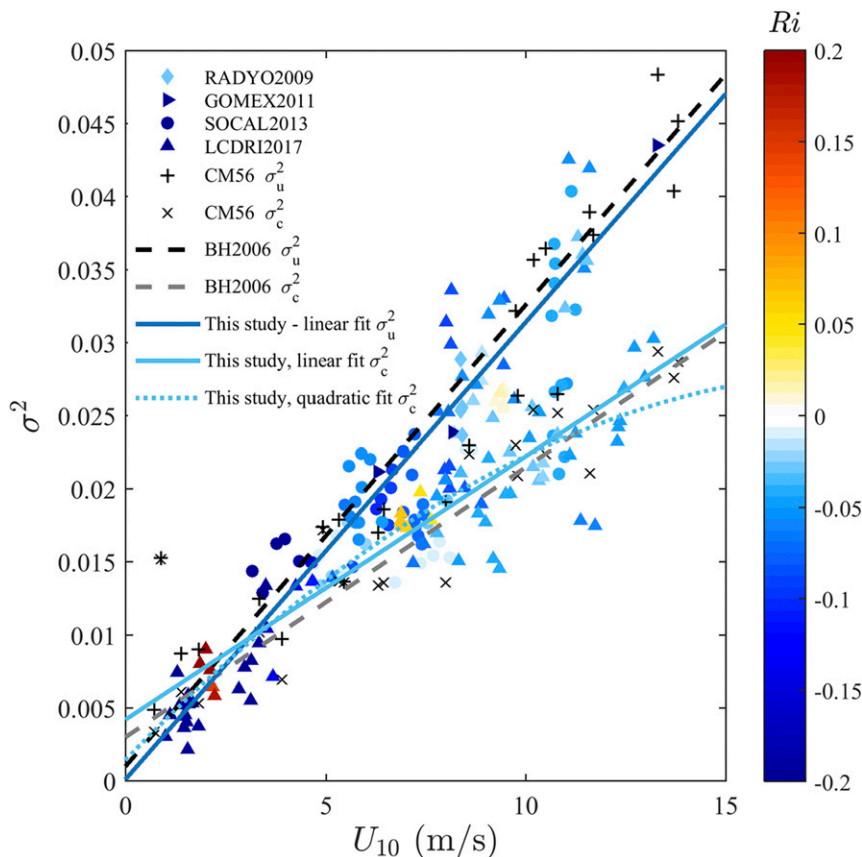


FIG. 6. The same data as in Fig. 3, but this time color coded for the nondimensional reduced Richardson number Ri .

detailed characterization of the atmospheric boundary layer was conducted from R/P *FLIP*, moored within 10 km of the data considered here. We find more scatter in the data plotted against u_* as compared with U_{10} , shown in Fig. 3. One would have anticipated more scatter with U_{10} caused by atmospheric stability variations that are not accounted for in the computation (Shaw and Churnside, 1997); however, u_* is a noisier measurement than U_{10} , and therefore perhaps this is not completely unexpected. Linear fits are computed for both upwind and crosswind components, giving

$$\sigma_u^2 = 7.92 \times 10^{-2} u_* + 9.02 \times 10^{-4} \quad \text{and} \quad (14)$$

$$\sigma_c^2 = 4.86 \times 10^{-2} u_* + 3.77 \times 10^{-3}. \quad (15)$$

From these relationships, the slope distribution statistic computed from the airborne lidar instrument can be used to estimate U_{10} and u_* . This application is described in the appendix, along with a surface-wave spectrum-based technique to compute the wind direction.

c. Atmospheric stability

For consistency with past studies, we use here a reduced Richardson number Ri to characterize the atmospheric stability, given by

$$Ri = g \frac{(T_a - T_w)z}{T_w U_z^2}, \quad (16)$$

where g is the gravitational acceleration, T_a is the atmospheric temperature at the anemometer height z , T_w is the water temperature at the surface, and U_z is the horizontal wind speed. Figure 6 shows the mean-square slope results plotted against wind speed, similar to Fig. 3, but this time color coded for Ri . The bulk of the measurements considered here correspond to conditions from neutral to unstable (negative Ri), with very few instances of stable conditions (positive Ri).

Following the Shaw and Churnside (1997) approach, the ratio of the measured mean-square slope and the Cox and Munk (1954) modeled mean-square slope, or σ^2/σ_{cm}^2 , is shown in Fig. 7 plotted against Ri ,

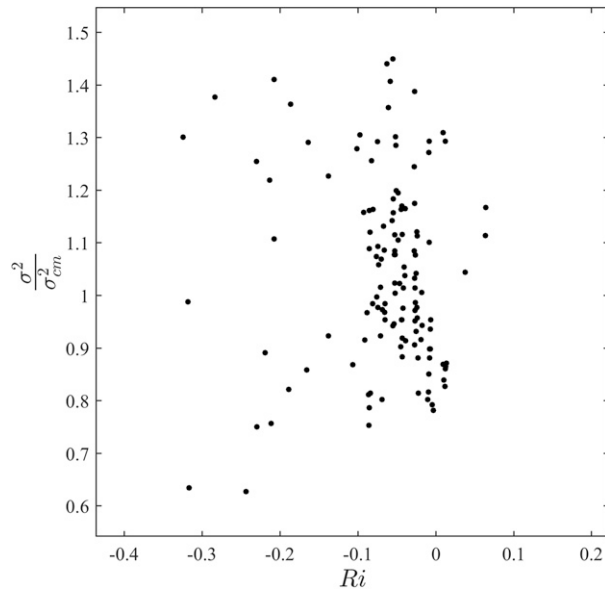


FIG. 7. Measured mean-square slope normalized by the model of Cox and Munk (1954) against Ri , which is a measure of atmospheric stability. No clear effects from the atmospheric stability are found.

for both cross- and upwind cases to highlight any stability dependence. Here σ_{cm}^2 is calculated for each sample based on its heading information and the appropriate cross- or upwind model from Cox and Munk (1954). While Shaw and Churnside (1997) had identified a relationship between mean-square slope and stability, no clear trend is found in the present study.

d. Higher-order statistics

The normalized skewness χ is computed from the third moment of the discrete distribution p , defined as

$$\chi = \chi_s / \sigma^3, \quad (17)$$

where

$$\chi_s = \sum_{i=1}^N (m_i - \mu)^3 p(m_i) \Delta m. \quad (18)$$

The normalized skewness χ is also equivalent to the expansion coefficients of a Gram–Charlier distribution c_{03} and c_{21} for upwind and crosswind components, respectively (Papoulis and Pillai, 2002; Munk, 2009). Figure 8 shows χ plotted against U_{10} , color coded for heading relative to the mean wind direction, along with the expansion coefficients c_{03} and c_{21} from Cox and Munk (1954) and Bréon and Henriot (2006). Unlike these prior studies, we do not

find significant skewness of the measured slope pdfs. The magnitude of χ is generally smaller than 0.1, with no clear relationship with wind speed, as previously found in other studies.

The excess kurtosis ψ is computed from the fourth moment of the discrete distribution p , defined as

$$\psi = (\psi_s / \sigma^4) - 3, \quad (19)$$

where

$$\psi_s = \sum_{i=1}^N (m_i - \mu)^4 p(m_i) \Delta m. \quad (20)$$

For comparison purposes, the excess kurtosis is equivalent to the expansion coefficients of a Gram–Charlier series c_{40} and c_{04} for upwind and crosswind components, respectively. Figure 9 shows ψ plotted against wind speed U_{10} , color coded for heading relative to the mean wind direction, along with the expansion coefficients c_{40} and c_{04} from Cox and Munk (1954) and Bréon and Henriot (2006). Although the magnitude of ψ is not consistent with these studies, we find ψ to decrease with wind speed, at different slopes for crosswind (blue points) and upwind (red points) directions.

It is intriguing to find such discrepancies among these three studies for the higher-order statistics presented here while the agreement for the mean-square slope is very good. Looking closely at the data from Figs. 8 and 9, we find some agreement, in magnitude and sign, among Cox and Munk (1954), Bréon and Henriot (2006), and the current study for wind speeds lower than approximately $4\text{--}5 \text{ m s}^{-1}$. Interestingly, this is also the wind speed at which aerated wave breaking is often considered to begin. An important assumption in the derivation of the slope statistics from reflectance measurements is the need to filter out all foam and breaking waves from the collected data. This was a known challenge in Cox and Munk’s (1954) seminal work (C. Cox 2014, personal communication), in which whitecaps were removed manually, where possible. The Bréon and Henriot (2006) approach consisted of removing data for which contributions from foam and aerosols were found to be larger than an empirical threshold, based on the off-glint measurements (reflectance greater than 10^{-2}). Removing the whitecaps and foam contribution to the reflectance is particularly challenging with the POLDER dataset, because the ground size of a measured pixel is large—for example, $6 \times 7 \text{ km}^2$ at nadir (Deschamps et al. 1994).

The obvious question that arises then is whether the relationship between wind speed and skewness, and to

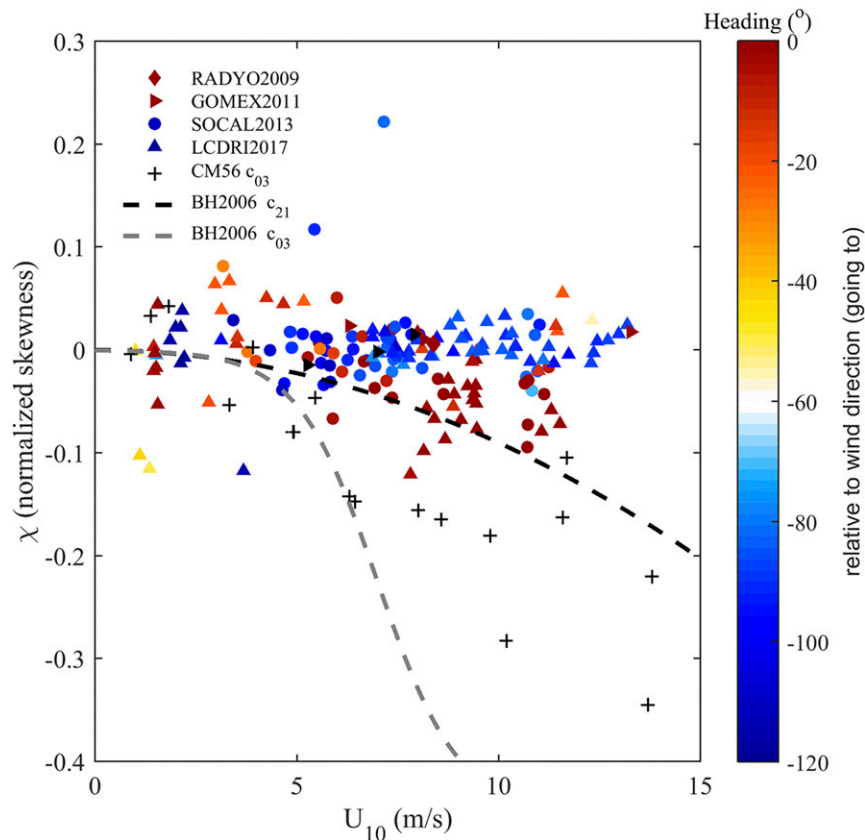


FIG. 8. Normalized skewness χ computed from the airborne lidar during four distinct experiments (RADYO2009, GOMEX2011, SOCAL2013, and LCDRI2017), color coded for their heading relative to the mean wind direction, along with the data from Cox and Munk (1954) and Bréon and Henriot (2006), as a function of U_{10} .

some extent kurtosis, found in the reflectance-based retrieval technique is a measurement artifact, resulting from inhomogeneities in the properties of the whitecap and foam spatial coverage, such as variation in whitecap fraction on the forward and rear face of breaking surface waves or modulation of shorter breaking waves by longer waves. This is a research topic we are actively pursuing but is not within the scope of the work presented here.

4. Discussion and summary

In this study, surface slope statistics were computed from airborne scanning topographic lidar data that were collected during a series of field experiments off the coast of California and in the Gulf of Mexico over a broad range of environmental conditions, with wind speeds ranging from approximately 1–2 up to 13 ms^{-1} . The technique used here differs from the reflectance-based approach of Cox and Munk (1954) and instead derives the slope distribution by counting laser glints

produced by specular reflections as the lidar is scanned over the surface of the ocean. Overall, we find good agreement with the results of Cox and Munk (1954) and the more recent results of Bréon and Henriot (2006) that are based on satellite remote sensing products for the mean-square slope. Unlike Shaw and Churnside (1997) or Hwang and Shemdin (1988), we do not find any obvious correlations between the mean-square slope and the atmospheric stability, at least for the neutral and unstable conditions experienced during the experiments considered here.

Significant discrepancies with past studies (Cox and Munk, 1954; Bréon and Henriot, 2006) are found for the higher-order statistics and remain to be explained. These are particularly difficult measurements to obtain through remote sensing techniques; in particular, the reflectance-based approach used by Cox and Munk (1954) and Bréon and Henriot (2006) requires filtering out the portion of the data that is contaminated by whitecap coverage, which is a challenging operation, especially for high wind cases. If not

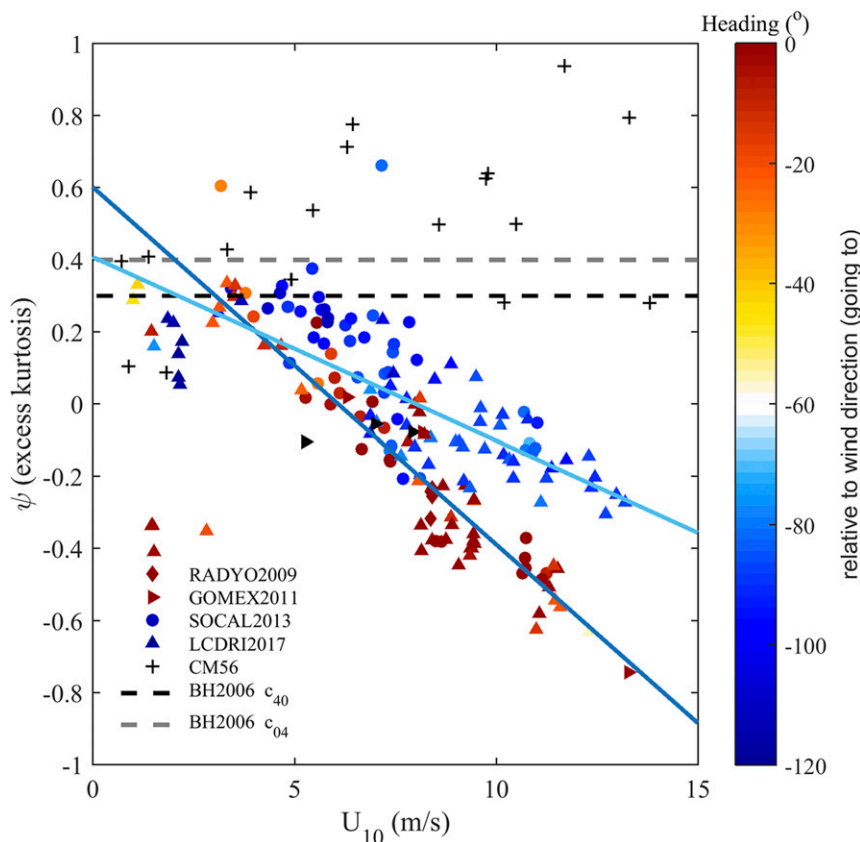


FIG. 9. As in Fig. 8, but for excess kurtosis ψ .

filtered out correctly (or completely), any skewness or excess kurtosis in the spatial properties of the whitecap coverage could lead to an erroneous slope distribution computation. This is not within the scope of this work but is a topic that we are actively pursuing.

As first identified more than 60 years ago by Cox and Munk in their seminal work, we find a linear wind dependence of the mean-square slope, with a large crosswind component of the slope observed for winds greater than $3\text{--}4\text{ m s}^{-1}$ that corresponds to approximately 70%–90% of the upwind component, depending on the wind speed. To this end, no theory has been brought forward that would explain such surface slope statistics, and in particular such a large crosswind component. Munk proposed that localized sources, such as pressure points, could generate obliquely propagating waves (cf. Kelvin ship waves).

Recent progress in our understanding of the directionality of the surface wave spectrum, highlighting the transition from unimodal to bimodal spectral distribution in wind-generated surface waves (Banner and Young 1994; Leckler et al. 2015; Lenain and Melville 2017; Peureux et al. 2018), is now bringing us a step

closer to solving this problem. The mechanisms that lead to a wide bimodal surface wave spectrum remain unclear; standard gravity wave modeling using four-wave resonance is just an asymptotic model, and for larger times and larger slopes five-and-higher-wave resonances are possible. Su et al. (1982) and Melville (1982) showed direct evidence of the growth of crescent-shaped waves in laboratory experiments, for larger wave slopes, as the result of five-wave interactions that lead to three-dimensional instabilities that are stronger than the two-dimensional Benjamin–Feir instabilities (McLean et al. 1981). Wave breaking also needs to be considered as a source of wave components traveling in almost transverse or even upstream directions (Rapp and Melville 1990). As far as we are aware, there has not been any modeling of the effects of the directional distribution of wave breaking on surface slope statistics. The source of the large crosswind component of the mean-square slope therefore remains elusive, but the evidences presented here calls for more spatiotemporal measurements of surface waves and wave breaking, at very small scales, from $O(1\text{ mm})$ to $O(10\text{ m})$ in particular, and modeling of higher-order wave–wave interactions.

We also demonstrate here that airborne scanning lidar technology is a viable tool to measure mean-square slope and to estimate surface wind speed and momentum flux remotely. This is of importance, because the availability of surface wind measurements is often limited to buoys or vessel-mounted instrumentation that usually provides poor spatial coverage and satellite remote sensing products do not have the flexibility or the spatial and temporal resolution needed for studies on submesoscales and smaller. This approach, along with the development of new technology (Rodríguez et al. 2018a,b) that is capable of significantly better spatial resolution, can further enhance our understanding of the underlying physical processes driving the spatiotemporal variability of surface winds from submesoscale to kilometer scale. This is particularly relevant for wave forecasting, because it is now well accepted that the largest errors in wave predictions are often caused by a lack of accurate momentum flux estimates (Janssen 2004). The measurement approach proposed here provides a means of improving local measurements of wind variability and, in turn, wave prediction capabilities, in areas ranging from coastal to open ocean waters.

Acknowledgments. The initial motivation for this work came from the need to measure the wind forcing beneath the footprint of the Modular Aerial Sensing System (Melville et al. 2016). The authors gratefully acknowledge numerous discussions with Charles “Chip” Cox and Walter Munk prior to their deaths in 2017 and 2019, respectively. The authors are grateful to Aspen Helicopter for providing flight resources. We are thankful to Laurent Grare for providing the atmospheric data collected from R/P *FLIP* and for helpful discussions. We are thankful to Luigi Cavaleri (from ISMAR in Venice, Italy) for his suggestions, which improved the paper. This research was supported by grants to WKM from the Physical Oceanography programs at ONR (Grants N00014-17-1-2171, N00014-14-1-0710, and N00014-17-1-3005) and NSF (OCE; Grant OCE-1634289) and from industry.

APPENDIX

Altitude Correction, Wind Speed Validation, and Wind Direction Retrieval

a. Altitude correction

All lidar measurements presented here are initially range corrected to take into account any changes in the received laser signal amplitude \mathcal{A}_r that are associated

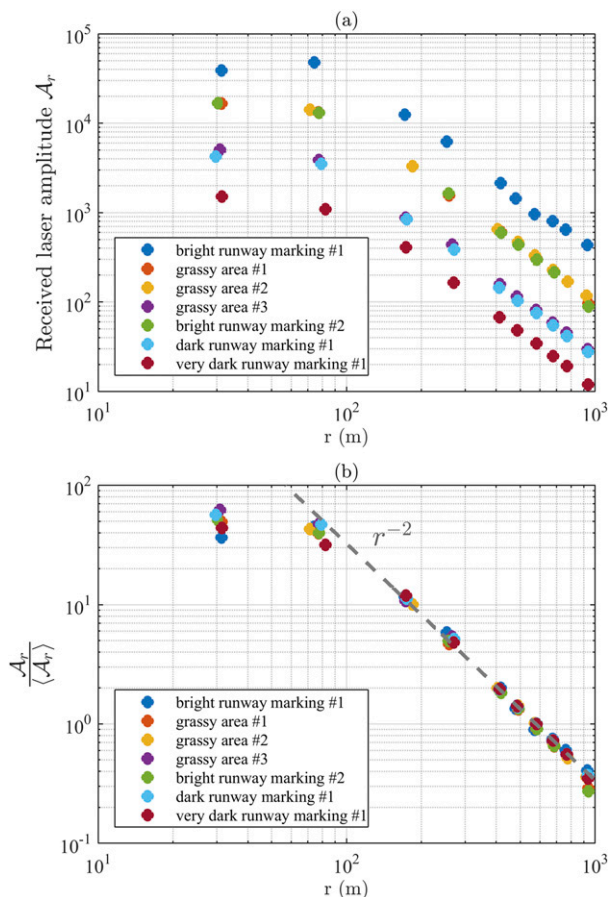


FIG. A1. (a) Backscattered laser amplitude \mathcal{A}_r , as a function of altitude r , at nadir, for a range of targets. (b) The same data, but now scaled by the mean amplitude $\langle \mathcal{A}_r \rangle$, computed for $r > 100$ m.

with variations in the distance between the instrument and the measurement target within a single scan, and between flights that are conducted at different altitudes. The MASS lidar, a Riegl Q680i instrument, was range-calibrated during a series of flights on 31 July 2015, in Oxnard, California. The MASS was installed on a Bell 206-L III Long Ranger helicopter operated by Aspen Helicopter. Stationary flights were conducted at altitudes ranging from 30 to 1000 m over a variety of targets (e.g., runway markings and grassy areas) to cover a broad range of backscatter amplitudes, corresponding to the known range of amplitude \mathcal{A}_r that has been measured over the ocean surface in this study. Figure A1 shows the received laser amplitude \mathcal{A}_r as a function of altitude r , at nadir, for these targets. We find a clear r^{-2} power law for $r > 100$ m, the lowest altitude from which we typically collect data, such that

$$\mathcal{A}_{rc} = (r_{\text{ref}}/r)^2 \mathcal{A}_r, \quad (\text{A1})$$

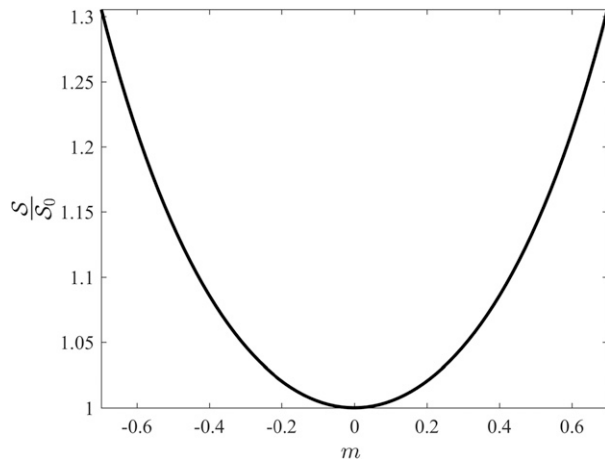


FIG. A2. Fraction of the surface area of the laser footprint S normalized by the surface area of the footprint at nadir S_0 as a function of viewing angle m , in radians. We find an increase in the area of the footprint of up to 30% at the edges of the lidar swath, which ranges here over $\pm 30^\circ$ from nadir ($m = 0$) in the cross-track direction.

where the reference altitude r_{ref} is arbitrarily set to 300 m. In addition, the received amplitude is also corrected for changes in the ellipsoidal area S of the laser footprint as a function of scanning angle, for a given scan, as illustrated in Fig. A2:

$$\mathcal{A}_{rc2} = \frac{r^2(\theta)}{r^2(0)} \cos\theta \mathcal{A}_{rc}. \quad (\text{A2})$$

Last, to account for a remaining altitude dependence in our measurements that is likely associated with multipath returns within the footprint of the lidar for which we cannot formally account, a final correction is applied by only considering in the analysis backscattered lidar returns of amplitude

$$\mathcal{A}_{rc2} > \alpha_0 \langle \mathcal{A}_{rc2} \rangle, \quad (\text{A3})$$

where α_0 is a threshold coefficient that is estimated iteratively by minimizing the scatter obtained in the slope variance measurements. Figure A3 shows the residual of the minimization process as a function of the threshold coefficient. Here α_0 is set to the value at the 95 percentile of the residual.

b. Lidar-derived wind speed validation

We can use the slope distribution statistics computed from the airborne lidar instrument to derive the wind speed U_{10} and friction velocity u_* . This is of significance because in situ surface wind measurements are usually very sparse, being collected from a limited number of

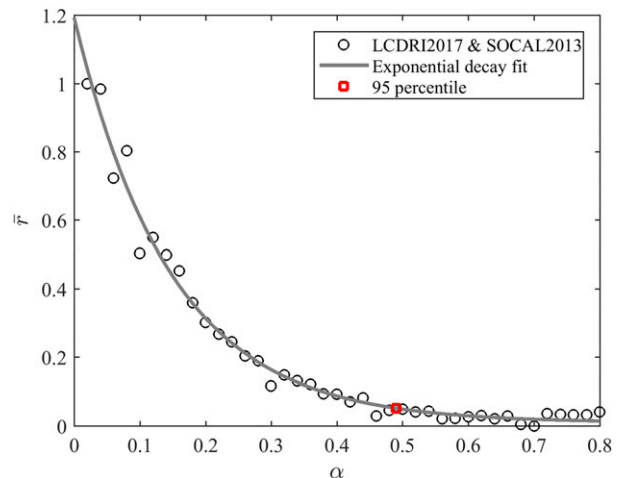


FIG. A3. Residuals \bar{r} from the scatter minimization process plotted against the amplitude threshold value α .

meteorological buoys, and satellite remote sensing products do not have the spatial resolution needed for studies on scales that are submesoscale and smaller.

This technique was tested during a series of experiments: the ONR funded Innershelf DRI program (2017), off Point Sal, California, the GoMEX experiment in the Gulf of Mexico (2011) and a SARAL/AltiKa overflight off the coast of central California (2015). None of the data from these experiments were included in the fitting of the mean-square slope and atmospheric forcing presented earlier, but they are used here.

Figure A4 shows the lidar estimates of wind speed U_{10} against coincident (within 10 min), collocated (within 2.5 km), independent measurements, either from in situ or satellite remote sensing products. Here the mean-square slope σ^2 that is computed from a 2.5-km airborne lidar transect is used to derive U_{10} . We find an RMS error ranging from 0.96 to 1.45 m s^{-1} for the upwind and crosswind directions, respectively, for each individual measurement. The black circles represent lidar-derived wind estimates plotted against in situ wind records collected during the Innershelf DRI program. Here the in situ data are based on a combination of three research vessels, each instrumented with a meteorological mast (R/V *Sally Ride*, R/V *Oceanus*, and R/V *Sproul*) and a nearshore surface buoy located southeast of Point Sal. The colored circles correspond to lidar-derived wind estimates plotted against surface wind data collected from two satellites, *Jason-1* and SARAL/AltiKa. The agreement is good with the satellite products, but we find some deviations between our estimate of U_{10} and the in situ measurements collected during the Innershelf DRI experiment described above. These might have been caused by errors in the in situ wind measurements

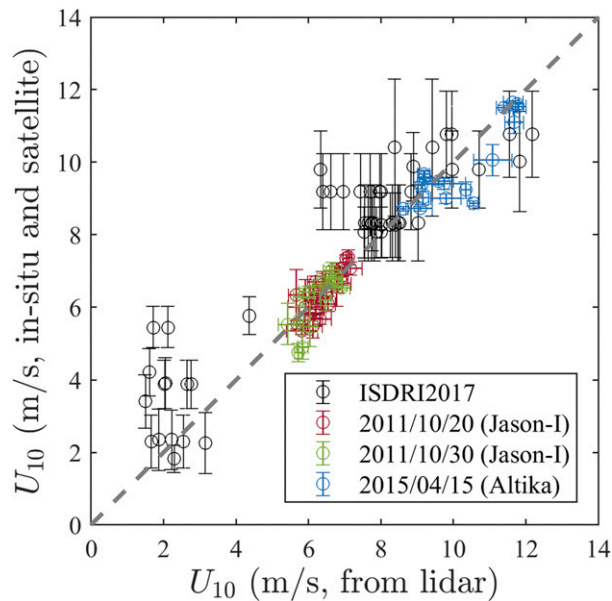


FIG. A4. Wind speed U_{10} as estimated from the airborne lidar measurements compared with collocated in situ (ISDRI2017) and satellite remote sensing products (*Jason-1* and *AltiKa*).

that can be associated with the flow distortion around the vessel, exacerbated by the low vessel speed (from stationary to $1\text{--}2\text{ m s}^{-1}$) imposed by the in-water component of ship operations for data collection, and repeated ship heading changes. This also highlights the challenges of collecting science-grade wind measurements from research vessels, despite various attempts to account for the flow distortion (e.g., [Miller et al. 2008](#); [Landwehr et al. 2015](#)), and the scientific need for other means of obtaining surface wind measurements. Overall we find a small bias of $+0.3\text{ m s}^{-1}$ for a 1:1 slope and a coefficient of determination $R^2 = 0.82$. This value goes up to 0.95 when only the satellite remote sensing products are considered, with a similar bias ($+0.35\text{ m s}^{-1}$).

[Figure A5](#) shows the lidar estimates of u_* against the same coincident (within 10 min), collocated (within 2.5 km), independent measurements that were presented in [Fig. A4](#). Here the friction velocity is computed iteratively using the Tropical Ocean and Global Atmosphere Coupled Ocean–Atmosphere Response Experiment 3.0 (TOGA COARE 3.0) algorithm assuming a constant flux layer with a logarithmic wind profile ([Fairall et al. 2003](#)). We find a small bias between the two estimates, $+0.035\text{ m s}^{-1}$, showing a slightly larger value of u_* with the lidar-based measurements, and a coefficient of determination $R^2 = 0.8$.

c. Wind direction retrieval

Because the wind direction cannot be retrieved from the lidar return statistics without conducting dedicated

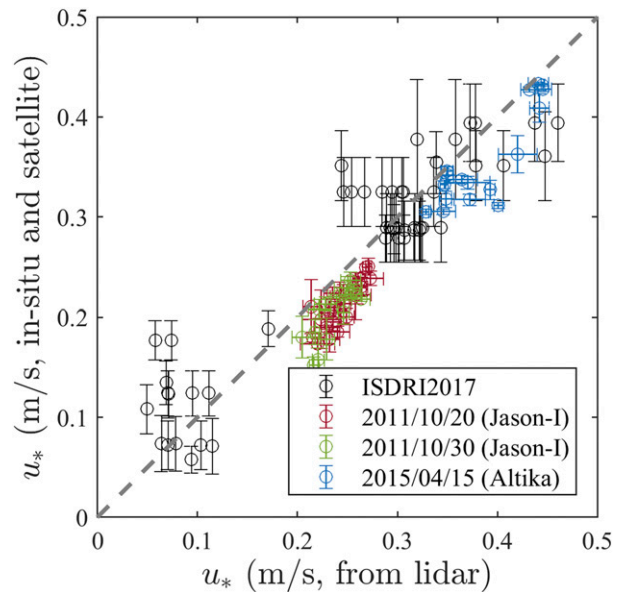


FIG. A5. As in [Fig. A4](#), but for friction velocity u_* and based on wind speed measurements and bulk formulation (TOGA COARE 3.0).

flights, for example, a star pattern over a short period of time to quantify the variability of mean-square slope σ^2 as a function of heading to relate it to the mean wind direction, here we utilize the directional spectral properties of the measured wind-generated surface waves. Note that this approach is only valid for wind speeds of greater than $2\text{--}3\text{ m s}^{-1}$ to ensure sufficient density of lidar returns required to compute the directional wave spectra.

Ten-kilometer-long swaths of georeferenced ocean surface topography data centered on R/P *FLIP* were interpolated on a regular grid, with the horizontal spatial resolution being a function of the flight altitude ([Lenain and Melville 2017](#)). Two-dimensional fast Fourier transforms were computed over 5-km segments with 50% overlap. All segments were first detrended, tapered with a two-dimensional Hanning window, and padded with zeros (25%). The obtained 2D spectra were corrected for Doppler shift induced by the relative motion between the phase speed of the waves and the aircraft velocity, using the method developed by [Walsh et al. \(1985\)](#).

[Lenain and Melville \(2017\)](#) highlighted the transition from unimodal to bimodal directional distribution found in wind-generated surface wave spectra [see [Figs. 3 and 4](#) of [Lenain and Melville \(2017\)](#) and the related discussion therein]. The wind direction is taken here as the direction of highest spectral density in the directional spectrum at the measured wavenumber corresponding to this transition. [Figure A6](#) shows the comparison

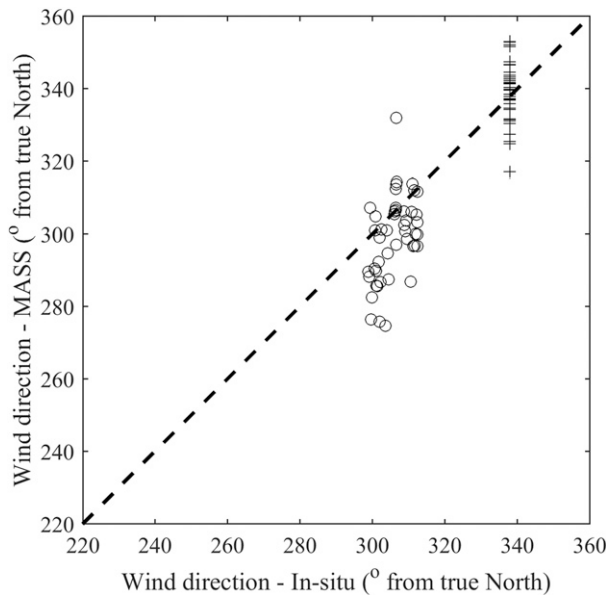


FIG. A6. Comparison between independent wind direction measurements and estimates derived from the directional wavenumber spectra. The open circles correspond to the LCDRI2017 experiment results, and the plus signs represent data collected during an AltiKa overflight off the coast of Monterey in April 2015.

between independent wind direction measurements and estimates derived from directional surface wavenumber spectra collected during the LCDRI2017 experiment, along with results from an AltiKa overflight in April 2015 off the coast of Monterey. In that latter case we used the standard wind direction product provided in the L2 level of the AltiKa dataset (AVISO; note that acronyms that are not defined in this paper may be found at <https://PubsAcronymList>). We find good agreement between in situ and lidar-based wind direction values, with an rms error of approximately 10° .

REFERENCES

- Abdalla, S., 2012: Ku-band radar altimeter surface wind speed algorithm. *Mar. Geod.*, **35**, 276–298, <https://doi.org/10.1080/01490419.2012.718676>.
- Banner, M., and I. Young, 1994: Modeling spectral dissipation in the evolution of wind waves. Part I: Assessment of existing model performance. *J. Phys. Oceanogr.*, **24**, 1550–1571, [https://doi.org/10.1175/1520-0485\(1994\)024<1550:MSDITE>2.0.CO;2](https://doi.org/10.1175/1520-0485(1994)024<1550:MSDITE>2.0.CO;2).
- Bréon, F., and N. Henriot, 2006: Spaceborne observations of ocean glint reflectance and modeling of wave slope distributions. *J. Geophys. Res.*, **111**, C06005, <https://doi.org/10.1029/2005JC003343>.
- Cox, C., 2015: Suppression of breakers in stormy seas by an oil film. *Int. J. Marit. Hist.*, **27**, 528–536, <https://doi.org/10.1177/0843871415588671>.
- , and W. Munk, 1954: Measurement of the roughness of the sea surface from photographs of the sun's glitter. *J. Opt. Soc. Amer.*, **44**, 838–850, <https://doi.org/10.1364/JOSA.44.000838>.
- , and —, 1956: Slopes of the sea surface deduced from photographs of sun glitter. *Bull. Scripps Inst. Oceanogr.*, **6**, 401–488.
- Cox, C. S., X. Zhang, and T. F. Duda, 2017: Suppressing breakers with polar oil films: Using an epic sea rescue to model wave energy budgets. *Geophys. Res. Lett.*, **44**, 1414–1421, <https://doi.org/10.1002/2016GL071505>.
- Deschamps, P.-Y., F.-M. Bréon, M. Leroy, A. Podaire, A. Bricaud, J.-C. Buriez, and G. Seze, 1994: The POLDER mission: Instrument characteristics and scientific objectives. *IEEE Trans. Geosci. Remote Sens.*, **32**, 598–615, <https://doi.org/10.1109/36.297978>.
- Dickey, T., and Coauthors, 2012: Introduction to special section on recent advances in the study of optical variability in the near-surface and upper ocean. *J. Geophys. Res.*, **117**, C00H20, <https://doi.org/10.1029/2012JC007964>.
- Fairall, C., E. F. Bradley, J. Hare, A. Grachev, and J. Edson, 2003: Bulk parameterization of air–sea fluxes: Updates and verification for the COARE algorithm. *J. Climate*, **16**, 571–591, [https://doi.org/10.1175/1520-0442\(2003\)016<0571:BPOASF>2.0.CO;2](https://doi.org/10.1175/1520-0442(2003)016<0571:BPOASF>2.0.CO;2).
- Fung, A. K., K.-S. Chen, and K. Chen, 2010: *Microwave Scattering and Emission Models for Users*. Artech House, 430 pp.
- Gatebe, C. K., M. D. King, A. I. Lyapustin, G. T. Arnold, and J. Redemann, 2005: Airborne spectral measurements of ocean directional reflectance. *J. Atmos. Sci.*, **62**, 1072–1092, <https://doi.org/10.1175/JAS3386.1>.
- Gordon, H. R., and M. Wang, 1992: Surface-roughness considerations for atmospheric correction of ocean color sensors. 1: The Rayleigh-scattering component. *Appl. Opt.*, **31**, 4247–4260, <https://doi.org/10.1364/AO.31.004247>.
- , and —, 1994: Retrieval of water-leaving radiance and aerosol optical thickness over the oceans with SeaWiFS: A preliminary algorithm. *Appl. Opt.*, **33**, 443–452, <https://doi.org/10.1364/AO.33.000443>.
- Grare, L., L. Lenain, and W. K. Melville, 2018: Vertical profiles of the wave-induced airflow above ocean surface waves. *J. Phys. Oceanogr.*, **48**, 2901–2922, <https://doi.org/10.1175/JPO-D-18-0121.1>.
- Haimbach, S., and J. Wu, 1985: Field trials of an optical scanner for studying sea-surface fine structures. *IEEE J. Oceanic Eng.*, **10**, 451–453, <https://doi.org/10.1109/JOE.1985.1145129>.
- Hughes, B., H. Grant, and R. Chappell, 1977: A fast response surface-wave slope meter and measured wind-wave moments. *Deep-Sea Res.*, **24**, 1211–1223, [https://doi.org/10.1016/0146-6291\(77\)90524-0](https://doi.org/10.1016/0146-6291(77)90524-0).
- Hwang, P. A., and O. H. Shemdin, 1988: The dependence of sea surface slope on atmospheric stability and swell conditions. *J. Geophys. Res.*, **93**, 13 903–13 912, <https://doi.org/10.1029/JC093iC11p13903>.
- Janssen, P., 2004: *The Interaction of Ocean Waves and Wind*. Cambridge University Press, 312 pp.
- Kiefhaber, D., C. J. Zappa, and B. Jähne, 2015: Influence of natural surfactants on short wind waves in the coastal Peruvian waters. *Ocean Sci. Discuss.*, **12**, 1291–1325, <https://doi.org/10.5194/osd-12-1291-2015>.
- Kleiss, J. M., and W. K. Melville, 2010: Observations of wave breaking kinematics in fetch-limited seas. *J. Phys. Oceanogr.*, **40**, 2575–2604, <https://doi.org/10.1175/2010JPO4383.1>.
- , and —, 2011: The analysis of sea surface imagery for whitecap kinematics. *J. Atmos. Oceanic Technol.*, **28**, 219–243, <https://doi.org/10.1175/2010JTECH0744.1>.

- Landwehr, S., N. O. Sullivan, and B. Ward, 2015: Direct flux measurements from mobile platforms at sea: Motion and airflow distortion corrections revisited. *J. Atmos. Oceanic Technol.*, **32**, 1163–1178, <https://doi.org/10.1175/JTECH-D-14-00137.1>.
- Laxague, N. J., B. K. Haus, D. Bogucki, and T. Özgökmen, 2015: Spectral characterization of fine-scale wind waves using ship-board optical polarimetry. *J. Geophys. Res. Oceans*, **120**, 3140–3156, <https://doi.org/10.1002/2014JC010403>.
- Leckler, F., F. Ardhuin, C. Peureux, A. Benetazzo, F. Bergamasco, and V. Dulov, 2015: Analysis and interpretation of frequency-wavenumber spectra of young wind waves. *J. Phys. Oceanogr.*, **45**, 2484–2496, <https://doi.org/10.1175/JPO-D-14-0237.1>.
- Lenain, L., and W. K. Melville, 2017: Measurements of the directional spectrum across the equilibrium saturation ranges of wind-generated surface waves. *J. Phys. Oceanogr.*, **47**, 2123–2138, <https://doi.org/10.1175/JPO-D-17-0017.1>.
- Lillibridge, J., R. Scharroo, S. Abdalla, and D. Vandemark, 2014: One- and two-dimensional wind speed models for Ka-band altimetry. *J. Atmos. Oceanic Technol.*, **31**, 630–638, <https://doi.org/10.1175/JTECH-D-13-00167.1>.
- McLean, J., Y. Ma, D. Martin, P. Saffman, and H. Yuen, 1981: Three-dimensional instability of finite-amplitude water waves. *Phys. Rev. Lett.*, **46**, 817, <https://doi.org/10.1103/PhysRevLett.46.817>.
- Melville, W. K., 1982: The instability and breaking of deep-water waves. *J. Fluid Mech.*, **115**, 165–185, <https://doi.org/10.1017/S0022112082000706>.
- , and P. Matusov, 2002: Distribution of breaking waves at the ocean surface. *Nature*, **417**, 58–63, <https://doi.org/10.1038/417058a>.
- , L. Lenain, D. R. Cayan, M. Kahru, J. P. Kleissl, P. Linden, and N. M. Stom, 2016: The modular aerial sensing system. *J. Atmos. Oceanic Technol.*, **33**, 1169–1184, <https://doi.org/10.1175/JTECH-D-15-0067.1>.
- Ménard, Y., and Coauthors, 2003: The Jason-1 mission special issue: Jason-1 calibration/validation. *Mar. Geod.*, **26**, 131–146, <https://doi.org/10.1080/714044514>.
- Miller, S. D., T. S. Hristov, J. B. Edson, and C. A. Friehe, 2008: Platform motion effects on measurements of turbulence and air–sea exchange over the open ocean. *J. Atmos. Oceanic Technol.*, **25**, 1683–1694, <https://doi.org/10.1175/2008JTECH0547.1>.
- Munk, W., 1955: High-frequency spectrum of ocean waves. *J. Mar. Res.*, **14** (4), 302–314, <http://images.peabody.yale.edu/publications/jmr/jmr14-04-05.pdf>.
- , 2009: An inconvenient sea truth: Spread, steepness, and skewness of surface slopes. *Annu. Rev. Mar. Sci.*, **1**, 377–415, <https://doi.org/10.1146/annurev.marine.010908.163940>.
- Papoulis, A., and S. U. Pillai, 2002: *Probability, Random Variables, and Stochastic Processes*. McGraw-Hill, 852 pp.
- Peureux, C., A. Benetazzo, and F. Ardhuin, 2018: Note on the directional properties of meter-scale gravity waves. *Ocean Sci.*, **14**, 41–52, <https://doi.org/10.5194/os-14-41-2018>.
- Rapp, R. J., and W. Melville, 1990: Laboratory measurements of deep-water breaking waves. *Philos. Trans. Roy. Soc. London*, **331A**, 735–800, <https://doi.org/10.1098/rsta.1990.0098>.
- Reineman, B. D., L. Lenain, D. Castel, and W. K. Melville, 2009: A portable airborne scanning lidar system for ocean and coastal applications. *J. Atmos. Oceanic Technol.*, **26**, 2626–2641, <https://doi.org/10.1175/2009JTECH0703.1>.
- Rodríguez, E., A. Wineteer, D. Perkovic-Martin, T. Gál, B. Stiles, N. Niamsuwan, and R. R. Monje, 2018a: Ocean surface currents and winds using Dopplerscatt. *2018 IEEE Int. Geoscience and Remote Sensing Symp.*, Valencia, Spain, IEEE, 1474–1476, <https://doi.org/10.1109/IGARSS.2018.8517656>.
- , —, —, —, B. W. Stiles, N. Niamsuwan, and R. R. Monje, 2018b: Estimating ocean vector winds and currents using a Ka-Band pencil-beam Doppler scatterometer. *Remote Sens.*, **10**, 576, <https://doi.org/10.3390/rs10040576>.
- Romero, L., L. Lenain, and W. K. Melville, 2017: Observations of surface wave–current interaction. *J. Phys. Oceanogr.*, **47**, 615–632, <https://doi.org/10.1175/JPO-D-16-0108.1>.
- Shaw, J. A., and J. H. Churnside, 1997: Scanning-laser glint measurements of sea-surface slope statistics. *Appl. Opt.*, **36**, 4202–4213, <https://doi.org/10.1364/AO.36.004202>.
- Su, M.-Y., M. Bergin, P. Marler, and R. Myrick, 1982: Experiments on non-linear instabilities and evolution of steep gravity-wave trains. *J. Fluid Mech.*, **124**, 45, <https://doi.org/10.1017/S0022112082002407>.
- Su, W., T. P. Charlock, and K. Rutledge, 2002: Observations of reflectance distribution around sunglint from a coastal ocean platform. *Appl. Opt.*, **41**, 7369–7383, <https://doi.org/10.1364/AO.41.007369>.
- Sutherland, P., and W. K. Melville, 2013: Field measurements and scaling of ocean surface wave-breaking statistics. *Geophys. Res. Lett.*, **40**, 3074–3079, <https://doi.org/10.1002/grl.50584>.
- Walsh, E., D. Hancock III, D. Hines, R. Swift, and J. Scott, 1985: Directional wave spectra measured with the surface contour radar. *J. Phys. Oceanogr.*, **15**, 566–592, [https://doi.org/10.1175/1520-0485\(1985\)015<0566:DWSMWT>2.0.CO;2](https://doi.org/10.1175/1520-0485(1985)015<0566:DWSMWT>2.0.CO;2).
- Zappa, C. J., M. L. Banner, H. Schultz, A. Corrada-Emmanuel, L. B. Wolff, and J. Yalcin, 2008: Retrieval of short ocean wave slope using polarimetric imaging. *Meas. Sci. Technol.*, **19**, 055503, <https://doi.org/10.1088/0957-0233/19/5/055503>.
- , —, —, J. R. Gemmrich, R. P. Morison, D. A. LeBel, and T. Dickey, 2012: An overview of sea state conditions and air-sea fluxes during RaDyO. *J. Geophys. Res. Oceans*, **117**, C00H19, <https://doi.org/10.1029/2011JC007336>.